PCCP

ROYAL SOCIETY OF CHEMISTRY

PAPER

View Article Online
View Journal | View Issue

Cite this: *Phys. Chem. Chem. Phys.*, 2021, **23**, 19673

The Dirac half-semimetal and quantum anomalous Hall effect in two-dimensional Janus $Mn_2X_3Y_3$ (X, Y = F, Cl, Br, I)†

Ping Li *[ab] and Zhi-Xin Guo*[ac]

Received 6th May 2021,
Accepted 4th August 2021

DOI: 10.1039/d1cp02000e

rsc.li/pccp

The quantum anomalous Hall (QAH) effect has been experimentally observed in magnetically-doped topological insulators. However, the QAH effect is only seen at extremely low temperatures due to the weak magnetic coupling, small band gap and low carrier mobility. Here, based on first-principles density functional theory, we predict that the Janus $Mn_2X_3Y_3$ (X, Y) = F, Cl, Br, I are high Curie temperature ferromagnets. Furthermore, we find that they are Dirac half-metals characterized by a Dirac cone in one spin channel with carrier mobilities comparable to freestanding germanene and a large band gap in the other spin channel except for $Mn_2F_3I_3$. Simultaneously, when the spin–orbital coupling interaction is considered, the Janus $Mn_2F_3Cl_3$, $Mn_2Cl_3Br_3$, and $Mn_2Br_3I_3$ exhibit a nontrivial band gap, indicating that they host a QAH phase. More interestingly, both the Chern number sign and the chiral edge current are tuned by changing the direction of magnetization. Moreover, we find that topological properties are related to the lattice constant and magnetocrystalline anisotropy. Our findings would suggest the possibility of not only realizing the QAH effect but also designing the flow direction of the edge current.

I. Introduction

The quantum Hall (QH) effect is a novel quantum topological state that is realized in the absence of time reversal symmetry (TRS).[1] The TRS is broken by an external magnetic field and its topological origin is uncovered by the quantized Hall conductance.[2] However, an external magnetic field is not necessary for the new QH state which was first proposed by Haldane.[3] The new QH effect realized in the absence of a magnetic field is called the quantum anomalous Hall (QAH) effect. Two-dimensional (2D) materials are a prerequisite for realization of the QAH effect. The QAH state is characterized by chiral edge states that enclose an insulating bulk.[4] The dissipationless unidirectional electrical current without the need for an external magnetic field provides fascinating applications in low energy consumption electronics and spintronics.[5]

Up to now, the enormous Chern insulators have been theoretically predicted, including $Hg_{1-y}Mn_yTe$ quantum wells,[6] magnetically-doped $(Bi,Sb)_2Te_3$ thin films,[7] graphene,[8–11] silicene,[12–15] germanene,[16] stanene,[16–18] transition metal oxides,[19–22] metal–organic frameworks,[23–25] transition metal halides,[26–29] and others.[30,31] Among these, only the V or Cr doped $(Bi,Sb)_2Te_3$ systems and van der Waals layered material $MnBi_2Te_4$ have been experimentally realized to exhibit the QAH effect.[32–35] Unfortunately, all the experimentally observed QAH effects are achieved at extremely low temperature ($\sim$1 K). It is a daunting challenge for device applications. Obviously, it would be meaningful to search for a large band gap and high Curie temperature (T_C) Chern insulator.

In this work, we predict that 2D Janus $Mn_2X_3Y_3$ (X, Y = F, Cl, Br, I) are high Curie temperature ferromagnets. We find that the magnetic anisotropy energy reaches up to 47.60 meV per cell for $Mn_2Br_3I_3$. Furthermore, spin-polarized band structure calculations show a Dirac half-metal except for $Mn_2F_3I_3$. The spin up bands are metallic with a Dirac cone at the high symmetry K point near the Fermi level, while spin down bands are insulating with a gap of $\sim$4 eV. Moreover, non-trivial band gaps are opened by spin–orbital coupling (SOC) for $Mn_2F_3Cl_3$, $Mn_2Cl_3Br_3$, and $Mn_2Br_3I_3$. The QAH effect is clearly confirmed by the calculated Chern number C = 1 and chiral edge states. More interestingly, the chiral edge currents and the sign of the Chern number can be tunable by changing the direction of magnetization. Recently, the successfully synthesized 2D Janus MoSSe[36,37] paved the way for verifying the QAH effect in $Mn_2X_3Y_3$. These results offer a platform for investigating the high-temperature QAH effect and potential applications in spintronics.

[a] *State Key Laboratory for Mechanical Behavior of Materials, Center for Spintronics and Quantum System, School of Materials Science and Engineering, Xi'an Jiaotong University, Xi'an, Shaanxi, 710049, China. E-mail: pli@xjtu.edu.cn, zxguo08@xjtu.edu.cn*
[b] *Key Laboratory for Computational Physical Sciences (Ministry of Eduction), Fudan University, Shanghai, 200433, China*
[c] *Key Laboratory of Polar Materials and Devices (Ministry of Education), East China Normal University, Shanghai, 200241, China*

† Electronic supplementary information (ESI) available. See DOI: 10.1039/d1cp02000e

II. Structures and computational methods

To investigate the electronic and magnetic structures, we implemented the Vienna *Ab initio* Simulation Package (VASP)[38,39] for the first-principles calculations based on density functional theory (DFT). The electron exchange–correlation functional was described by the generalized gradient approximation of the Perdew–Burke–Ernzerhof functional.[40] The plane-wave basis set with a kinetic energy cutoff of 500 eV was employed. Here, $12 \times 12 \times 1$ and $24 \times 24 \times 1$ Γ-centered k meshes are adopted for the structural optimization and the self-consistent calculations. To avoid unnecessary interactions between the monolayers, the vacuum layer was set to 20 Å. The total energy convergence criterion was set to be 10^{-6} eV. What's more, to describe the strongly correlated 3d electrons of the Mn atom, the GGA+U method was used.[41] The onsite Coulomb repulsion U of the Mn atom is set to 4 eV.[42,43] To confirm the structural stability, phonon spectra were calculated using a finite displacement approach as implemented in the PHONOPY code, in which a $4 \times 4 \times 1$ supercell was used.[44] An effective tight-binding Hamiltonian constructed from the maximally localized Wannier functions (MLWFs) was employed to explored the edge states.[45–47] The Mn-d and X-p orbitals were chosen in the wannierization process. Therefore, the edge states were calculated in a half-infinite boundary condition using the iterative Green's function method by the package WannierTools.[47,48]

III. Results and discussion

A. Structure and stability

As shown in Fig. 1(a), monolayer Janus $Mn_2X_3Y_3$ has a layered hexagonal structure. It can be seen that Janus $Mn_2X_3Y_3$ consists of three flat atomic layers, composed of a hexagonal Mn layer sandwiched between the X and Y layers with unequal distances. The $Mn_2X_3Y_3$ inversion symmetry has been broken with it showing mirror asymmetry relating to the Mn atomic layer. Each of the Mn atoms is surrounded by six first-nearest-neighbor X and Y atoms in an octahedral environment. Table 1 lists values of the lattice constants, the Mn–X/Y and Mn–Mn bond lengths, and Mn–X/Y–Mn angle.

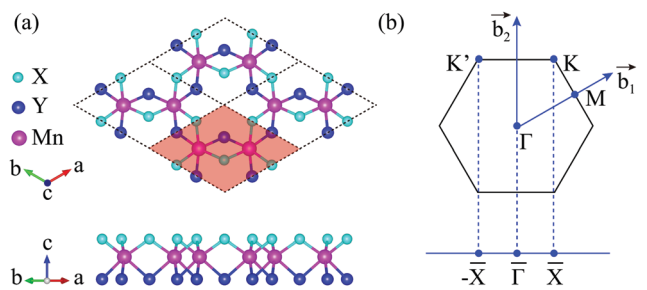

Fig. 1 (a) Top and side views of the lattice structure for the $Mn_2X_3Y_3$ monolayer, the unit cell is indicated by the magenta shading. The X, Y and Mn atoms are depicted by the light blue, dark blue and magenta balls, respectively. (b) The Brillouin zone of $Mn_2X_3Y_3$ with the reciprocal lattice vectors $\vec{b}_1$ and $\vec{b}_2$ and its projections onto the one-dimensional Brillouin zone.

Table 1 The lattice constant, bond lengths of Mn–X/Y and Mn–Mn, angle of the Mn–X/Y–Mn bond, the exchange energy J, cohesive energy and magnetocrystalline anisotropy (MCA) per unit area

	a (Å)	$d_{Mn-X/Y}$ (Å)	d_{Mn-Mn} (Å)	$\angle_{Mn-X/Y-Mn}$ (°)	J (meV)	E_c	MCA (erg cm^{-2})
$Mn_2F_3Cl_3$	5.78	1.98/2.38	3.34	114.43/89.16	3.08	3.62	−0.21
$Mn_2F_3Br_3$	6.05	2.01/2.38	3.49	120.83/80.68	3.28	3.46	−4.21
$Mn_2F_3I_3$	6.27	2.02/2.88	3.62	127.23/77.79	3.49	3.32	−1.46
$Mn_2Cl_3Br_3$	6.46	2.43/2.64	3.73	100.30/89.85	4.65	2.66	−4.56
$Mn_2Cl_3I_3$	6.64	2.40/2.79	3.83	106.08/86.62	4.75	2.60	−12.81
$Mn_2Br_3I_3$	6.82	2.55/2.78	3.94	100.86/90.12	4.83	2.38	−16.37

To characterize the thermodynamic stability of the Janus $Mn_2X_3Y_3$, we define the cohesive energy E_c as $E_c = (\sum N_i\mu_i - E_{tot})/N$. Here, μ_i is the chemical potential of i atom which is chosen to be the total energy of an isolated i atom. E_{tot} is the total energies of Janus $Mn_2X_3Y_3$. $N = \sum N_i\mu_i$, N_i and N and the numbers of i atoms and all atoms in the primitive unit cell, respectively. As shown in Table 1, the cohesive energy is ~3 eV per atom, which is larger than for Janus MoSSe (0.78 eV per atom).[49] The Janus MoSSe has recently been experimentally synthesized,[36,37] also indicating that Janus $Mn_2X_3Y_3$ could be synthesized experimentally. In order to confirm their thermodynamic stability, the lattice structure after annealing at 300 K for 3 ps displays that the $Mn_2X_3Y_3$ almost keeps the original structure unbroken. As shown in Fig. S1 (ESI†), the total energy fluctuates smoothly with time that further affirms its thermal stability. Furthermore, the dynamic stability of $Mn_2Cl_3Br_3$ is confirmed by its phonon spectrum without negative frequencies of the vibrational modes, as shown in Fig. S2 (ESI†).

B. The Curie temperature and magnetic anisotropy energy

The transition metal elements usually carry magnetic moments because of their partially filled d shell. The materials including Mn atom hence usually exhibit magnetic interactions, which is the case for Janus $Mn_2X_3Y_3$. As shown in Fig. 2(a), we consider all possible magnetic configurations in the 2×2 supercell, namely, the ferromagnetic (FM), antiferromagnetic-Néel (AFM-N), antiferromagnetic-stripy (AFM-ST), antiferromagnetic-zigzag (AFM-ZZ), antiferromagnetic-cluster-I (AFM-C-I), antiferromagnetic-cluster-II (AFM-C-II), and antiferromagnetic-cluster-III (AFM-C-III). Nonetheless, we find that the initial AFM-ST magnetic configuration always converges to the nonmagnetic state. It reveals that the metastable AFM-ST magnetic configuration does not exist in the system. As Table SI (ESI†) shows, the FM state has the lowest total energy. Therefore, the FM state is the ground state and has an integer magnetic moment of $8\mu_B$ per unit cell. This amounts to the $d^{4\uparrow 0\downarrow}$ spin configuration of Mn^{3+}, which can be verified by the Bader charge analysis.[50]

The Mermin–Wagner theorem points out that long-range magnetic order has been notably absent due to thermal fluctuations in 2D material.[51] However, there are two models that can exhibit magnetic order in 2D materials: the 2D XY model and

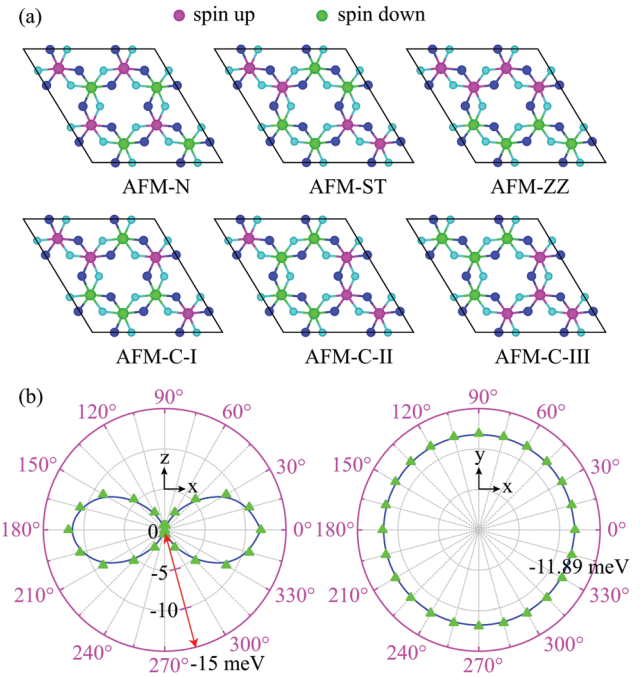

Fig. 2 (a) Top view of various AFM spin configurations: AFM-Néel (AFM-N), AFM-stripy (AFM-ST), AFM-zigzag (AFM-ZZ), AFM-cluster-I (AFM-C-I), AFM-cluster-II (AFM-C-II) and AFM-cluster-III (AFM-C-III), where the blue (green) circles denote the up (down) spins. (b) Angular dependence of the magnetic anisotropy energy (MAE) of $Mn_2Cl_3Br_3$ with the direction of magnetization lying on different planes (left) on the *xz* plane and (right) on the *xy* plane.

the Ising model. In the XY model, the spins show a preferred plane in the magnetic system. In this case, the material displays a quasi-long-range ordered phase at low temperature. The magnetization shows an easy axis in the Ising model. For this case, the material displays a second order phase transition to a magnetically ordered phase. Hence, where the 2D material shows a magnetically ordered phase, it relies on the magnetic anisotropy energy (MAE).

Here, we take $Mn_2Cl_3Br_3$ as an example. We consider two magnetization directions, namely, the in plane ([100] direction) and out of plane ([001] direction). The SOC is included in all the energy calculations. The MAE is defined as $\Delta E = E_{100} - E_{001}$. The negative value of the MAE shows the easy axis is along the *x* axis rather than along the *z* axis. The MAE is −11.89 meV per cell, indicating the magnetization along the *x* axis. Moreover, this also implies that $Mn_2Cl_3Br_3$ belongs to the category of XY magnet. It is eight times greater than that of 2D CrI_3 (1.37 meV per cell).[52] More interestingly, the experiment reported that the magnetization direction of 2D ferromagnets could be tuned by an external field in the Fe_3GeTe_2 system.[53]

Based on the octahedral symmetry of Janus $Mn_2Cl_3Br_3$, the angular dependence of the MAE can be described using the equation:

$$\mathrm{MAE} = K_1\cos^2\theta + K_2\cos^4\theta, \quad (1)$$

where K_1 (42.90 meV) and K_2 (−31.01 meV) are the MAE constants and θ is the azimuthal angle of rotation. As shown in Fig. 2(b), the MAE of Janus $Mn_2Cl_3Br_3$ in the *xz* plane can be fitted very well by this equation. The MAE shows a strong dependence on the *xz* plane, while exhibiting a weak dependence on the *xy* plane. It confirms again the strong magnetic anisotropy in the system.

As is well-known, the Curie temperature (T_C) of the ferromagnetic material positively correlates with its MAE. The large MAE indicates that high T_C can be anticipated in Janus $Mn_2X_3Y_3$. Hence, based on the Heisenberg model, we estimate the Curie temperature by using Monte Carlo (MC) simulations. The nearest neighbor exchange interaction parameters *J* can be described by the Hamiltonian of the Heisenberg model:

$$H = -\sum_{i,j} JS_i \cdot S_j - \sum_i AS_{iz}^2, \quad (2)$$

where *S* is the spin magnetic moment per Mn atom, *i* and *j* stand for the nearest site pairs. *A* is the anisotropy parameter. The exchange interaction parameter *J* is defined from the exchange energy as $J = E_{ex}/6S^2$, where $E_{ex} = (E_{AFM} - E_{FM})$ is the energy difference between the AFM-N and FM states. Therefore, the exchange interaction parameter *J* can be obtained, as listed in Table SI (ESI†). The exchange interaction increases from 3.08 meV for $Mn_2F_3Cl_3$ to 4.83 meV for $Mn_2Br_3I_3$. Here, the MC simulations are implemented on a 80 × 80 supercell which is adopted to reduce translational constraint, using 1×10^7 loops for each temperature. The simulated magnetic moment and spin susceptibility of $Mn_2X_3Y_3$ with respect to temperature are shown in Fig. 3. We find that T_C increases from 210 K for $Mn_2F_3Cl_3$ to 384 K for $Mn_2Br_3I_3$. It is significantly higher than CrI_3 (45 K).[54]

C. Electronic band structure

We next investigate the electronic band structure. The spin-polarized band structure is displayed in Fig. 4 and Fig. S3 (ESI†). The PBE+*U* and HSE06 results are shown in the upper panels and lower panels, respectively. The magenta and blue curves represent spin up and spin down bands, Remarkably, the Janus $Mn_2X_3Y_3$ are 100% spin-polarized Dirac half-metals except $Mn_2F_3I_3$. The spin up bands are metallic with a Dirac cone at the high symmetry *K* point near the Fermi level, while

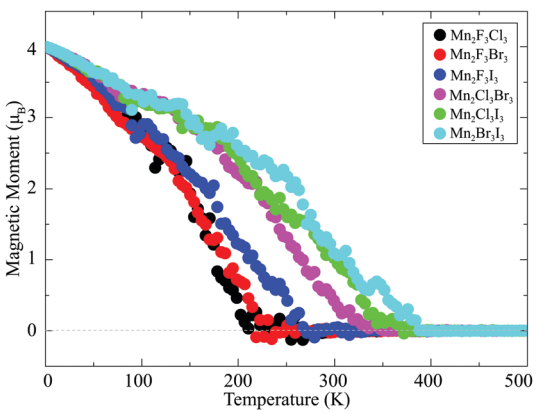

Fig. 3 Monte Carlo simulations of the average magnetic moment per unit cell with respect to the temperature calculated for $Mn_2X_3Y_3$.

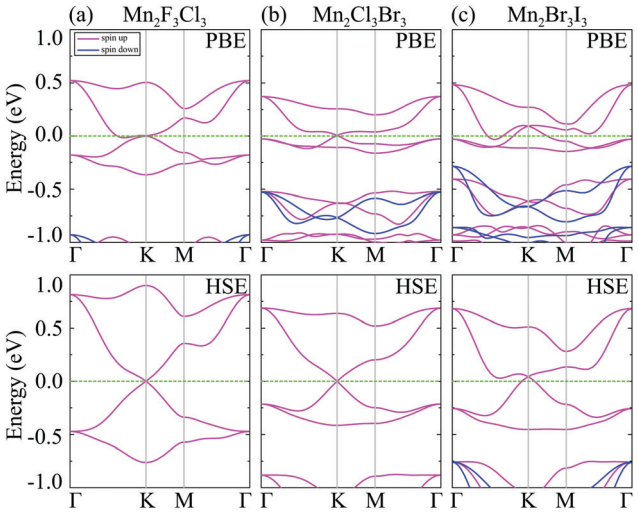

Fig. 4 Spin-polarized band structures of (a) $Mn_2F_3Cl_3$, (b) $Mn_2Cl_3Br_3$, and (c) $Mn_2Br_3I_3$ using the PBE+U and HSE06 methods. Spin up and spin down bands are plotted as magenta and blue curves, respectively.

spin down bands are insulating with a gap of ~4 eV. Furthermore, the HSE06 values of the Fermi velocity are acquired from the linear-like energy dispersion, with values of $(\partial\varepsilon/\partial k)\hbar^{-1}$ = 3.79 × 10^5, 1.20 × 10^5, and 1.15 × 10^5 for $Mn_2F_3Cl_3$, $Mn_2Cl_3Br_3$, and $Mn_2Br_3I_3$.[55] This is close to the value of 5.50 × 10^5 m s^{-1} in freestanding germanene.[56] The combination of massless Dirac fermion and 100% spin-polarized electron render a candidate for future application in optoelectronics and spintronics.

When the SOC is included, these Dirac cones become gapped, as shown in Fig. 5. The band structures of $Mn_2F_3Cl_3$, $Mn_2Cl_3Br_3$, and $Mn_2Br_3I_3$ are calculated by PBE+U and HSE06 methods. It is obvious that the band gaps are seriously underestimated by PBE+U. Band gaps of 11.7–95.6 meV are opened from $Mn_2F_3Cl_3$ to $Mn_2Br_3I_3$.

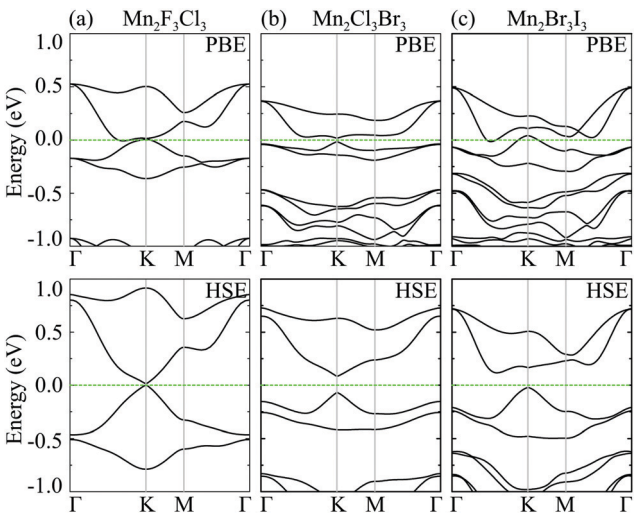

Fig. 5 Band structures of (a) $Mn_2F_3Cl_3$, (b) $Mn_2Cl_3Br_3$, and (c) $Mn_2Br_3I_3$ with SOC using the PBE+U and HSE06 methods.

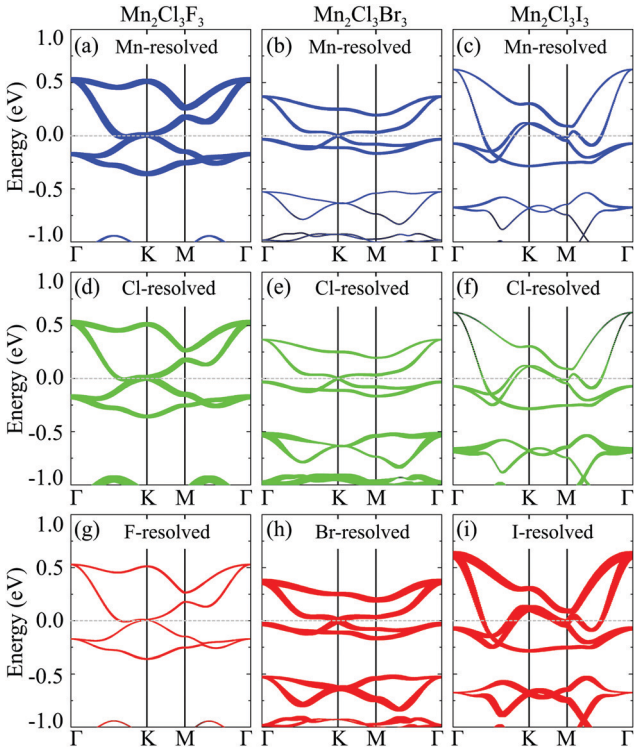

Fig. 6 Energy and k contribution of $Mn_2Cl_3F_3$ ($Mn_2F_3Cl_3$) (a, d and g), $Mn_2Cl_3Br_3$ (b, e and h) and $Mn_2Cl_3I_3$ (c, f and i) resolved to the spin up bands. (a–c) Mn atoms resolved band structures, (d–f) Cl atoms resolved band structures, and (g–i) F, Br and I atoms resolved band structures.

To understand the origin of Dirac states in the Janus $Mn_2X_3Y_3$, we resolve the orbitals of the spin up band structures for $Mn_2Cl_3Br_3$, as shown in Fig. S4 (ESI†). One can see that the Dirac states are mainly contributed by the Br $p_{x,y}$, and a little by the Cl $p_{x,y}$ and Mn $d_{xz,yz}$ orbitals. The $p_{x,y}$ Dirac states are particularly robust due to the nature of strong σ bonds.[15] The feature is different from the p_z Dirac states because of the nature of weak π bonds.[57,58]

Moreover, taking $Mn_2Cl_3F_3$ ($Mn_2F_3Cl_3$), ($Mn_2Cl_3Br_3$), and ($Mn_2Cl_3I_3$) as examples, we resolve the atoms of the spin up band structures, as shown in Fig. 6. We find that the contribution of halogen atoms gradually increases and the contribution of Mn atoms gradually decreases to Dirac states from $Mn_2Cl_3F_3$ to $Mn_2Cl_3I_3$. More interestingly, the Dirac states mainly come from halogen elements with large atomic numbers. This further confirms the Dirac states are formed by the hybridization of the d-orbital of Mn and the p-orbital of halogen atoms.

D. Quantum anomalous Hall effect

We know that the easy magnetization axis is the x axis from the MAE analysis. Hence, we take $Mn_2Cl_3Br_3$ as an example to study topological properties. When the SOC interaction is considered, we first calculate the magnetization direction along the x axis of band structure, as shown in Fig. 7(a). The band gap opens to 32.49 meV. When the magnetization direction is tuned to the z axis, the band gap enlarges to 28.38 meV, as shown in Fig. 7(c). From the above results, we know that the Dirac cone opens the

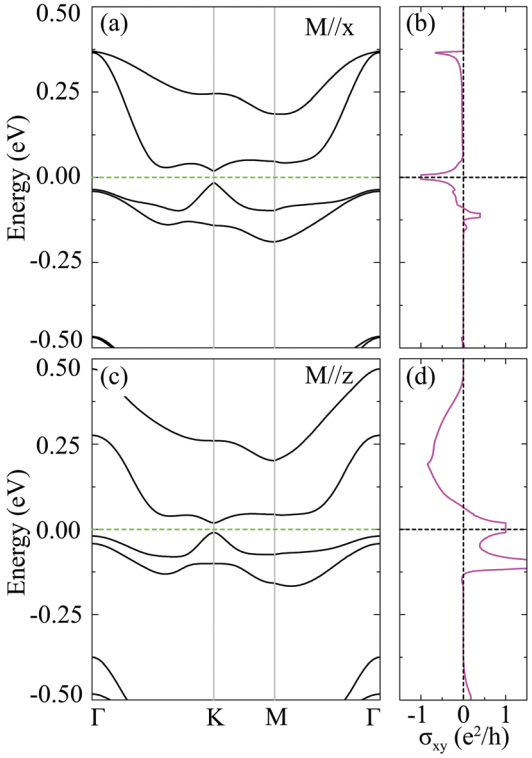

Fig. 7 Band structures of $Mn_2Cl_3Br_3$ with SOC as well as anomalous Hall conductivity (σ_{xy}) of the magnetization along the x-axis (a and b) and the magnetization along the z-axis (c and d).

band gap whether the magnetization direction is along the z or x axis, considering the SOC effect. These pave the way for the topological properties of the Janus $Mn_2Cl_3Br_3$.

To ensure the topological properties of Janus $Mn_2Cl_3Br_3$, we calculate the anomalous Hall conductivity (AHC) by using the formula

$$\sigma_{xy} = C\frac{e^2}{h}, \tag{3}$$

$$C = \frac{1}{2\pi}\int_{BZ} \mathrm{d}^2k\Omega(k), \tag{4}$$

where C is related to the anomalous Hall conductance σ_{xy}, namely, the Chern number.[59] The right panel of Fig. 7 shows the σ_{xy} relative to the Fermi level. The σ_{xy} shows a quantized value with $C = -1$ when the magnetization direction is along the x axis, confirming the Chern insulator. More interestingly, when the magnetization direction is tuned to the z axis, the Chern number changes to $C = 1$. It implies that the direction of the chiral edge current can be tuned by the changed magnetization direction.

In addition,

$$\Omega(k) = -\sum_n f_n \sum_{n' \neq n} \frac{2\mathrm{Im}\langle\psi_{nk}|v_x|\psi_{n'k}\rangle\langle\psi_{n'k}|v_y|\psi_{nk}\rangle}{(E_{n'} - E_n)^2}, \tag{5}$$

where $\Omega(k)$ is the Berry curvature in the reciprocal space, v_x and v_y are operator components along the x and y directions and $f_n = 1$ for the occupied bands.[60] The Berry curvatures in the

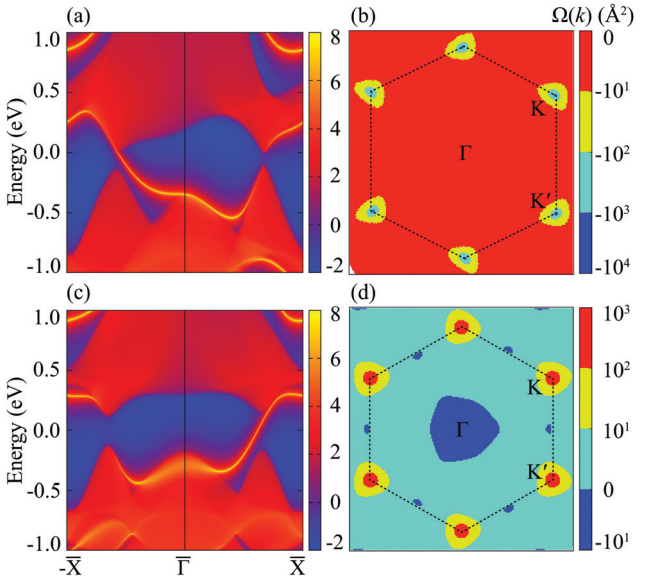

Fig. 8 Calculated edge state of a semi-infinite sheet and the Berry curvature of $Mn_2Cl_3Br_3$ of the magnetization along the x-axis (a and b) and the magnetization along the z-axis (c and d).

Brillouin zone are displayed in Fig. 8(b) and (d); the Berry curvature mainly shows around the K and K' points, which offer a QAH effect. The Berry curvatures have opposite signs when the magnetization directions are along the x and z axes. It is consistent with the opposite Chern values when the magnetization directions are along the x and z axis.

Another prominent characteristic of a Chern insulator is the existence of chiral edge states. Therefore, in order to further examine the topological properties, we constructed the Green's function of the $Mn_2Cl_3Br_3$ semi-infinite sheet from the MLWFs and calculated the local density of states at the edge, as shown in Fig. 8(a) and (c).[61,62] We can clearly see that one chiral edge state connects the valence and conduction bands. The direction of the chair edge current is opposite when the magnetization direction is along the x and z axis. Moreover, the number of edge states indicates the absolute value of the Chern number, which is $|C| = 1$.[63] What's more, the calculated FM ordering temperature is as high as 183 K for Janus $Mn_2Cl_3Br_3$. However, the band gap of 28.38–32.49 meV corresponds to 331–379 K. The temperature is large enough to retain the FM state. The conclusion is that the Janus $Mn_2Cl_3Br_3$ provides a promising platform for investigating the QAH effect at 183 K, which is three orders of magnitude higher than the temperature of 30 mK at which the QAH effect was recently observed in Cr-doped Bi_2Se_3 films.[32] Therefore, the Janus structure can be proved a QAH insulator.

Moreover, using the lattice constant (a) and MCA as the x and y coordinates, we can plot a topological phase of the 10 $Mn_2X_3Y_3$ as shown in Fig. 9, where the green and magenta regions are the convex envelopes of metals and TIs, respectively. We find that a smaller ratio of $|MCA/a|$ indicates that it is a topological insulator.

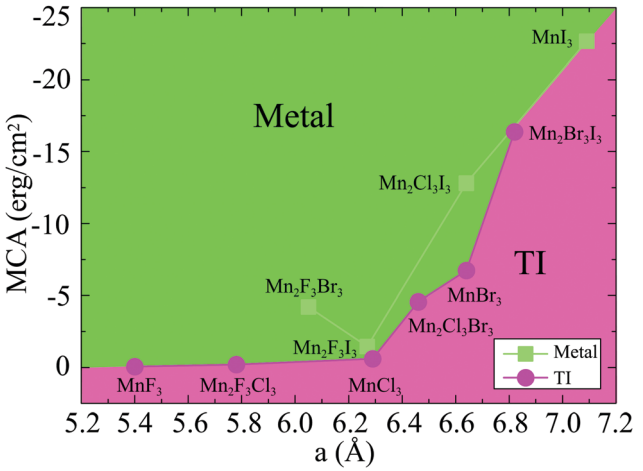

Fig. 9 Phase diagram for $Mn_2X_3Y_3$ using lattice constant and MCA. The metal and topological insulator (TI) phases are marked by the green and magenta areas.

IV. Conclusion

In summary, we predict that the Janus $Mn_2X_3Y_3$ is a Dirac half-metal which shows many intriguing properties, such as 100% spin polarization, large magnetic moment, large magnetic anisotropy energy, high Curie temperature, and massless Dirac fermion with high carrier mobility. When the spin–orbit coupling is considered, the Dirac cone opens the nontrivial topological band gap for $Mn_2F_3Cl_3$, $Mn_2Cl_3Br_3$, and $Mn_2Br_3I_3$. Remarkably, in the quantum anomalous Hall state both the chiral edge currents and the sign of the Chern number can be tuned by changing the direction of magnetization. Our work demonstrates the Janus $Mn_2F_3Cl_3$, $Mn_2Cl_3Br_3$, and $Mn_2Br_3I_3$ can realize a high-temperature QAH effect. Therefore, the Janus $Mn_2X_3Y_3$ provide great promise for applications in spintronic and electronic devices.

Conflicts of interest

There are no conflicts to declare.

Acknowledgements

This work is supported by the National Natural Science Foundation of China (No. 12004295 and No. 12074301), the Science Fund for Distinguished Young Scholars of Hunan Province (No. 2018JJ1022). P. Li thanks China's Postdoctoral Science Foundation funded project (No. 2020M673364) and the Open Project of the Key Laboratory of Computational Physical Sciences (Ministry of Education). This work was carried out at Lvliang Cloud Computing Center of China, and the calculations were performed on TianHe-2. Z. X. Guo thanks the Fundamental Research Funds for Central Universities (No. xzy012019062) and Open Research Fund of Key Laboratory of Polar Materials and Devices, Ministry of Education.

References

1 K. V. Klitzing, G. Dorda and M. Pepper, *Phys. Rev. Lett.*, 1980, **45**, 494.
2 D. J. Thouless, M. Kohmoto, M. P. Nightingale and M. denNijs, *Phys. Rev. Lett.*, 1982, **49**, 405.
3 F. D. M. Haldane, *Phys. Rev. Lett.*, 1988, **61**, 2015.
4 C. X. Liu, S. C. Zhang and X. L. Qi, *Annu. Rev. Condens. Matter Phys.*, 2016, **7**, 301.
5 H. M. Weng, R. Yu, X. Hu, X. Dai and Z. Fang, *Adv. Phys.*, 2015, **64**, 227.
6 C. X. Liu, X. L. Qi, X. Dai, Z. Fang and S. C. Zhang, *Phys. Rev. Lett.*, 2008, **101**, 146802.
7 R. Yu, W. Zhang, H. J. Zhang, S. C. Zhang, X. Dai and Z. Fang, *Science*, 2010, **329**, 61.
8 Z. H. Qiao, S. A. Yang, W. X. Feng, W. K. Tse, J. Ding, Y. G. Yao, J. Wang and Q. Niu, *Phys. Rev. B: Condens. Matter Mater. Phys.*, 2010, **82**, 161414(R).
9 J. Hu, J. Alicea, R. Wu and M. Franz, *Phys. Rev. Lett.*, 2012, **109**, 266801.
10 H. Zhang, C. Lazo, S. Blugel, S. Heinze and Y. Mokrousov, *Phys. Rev. Lett.*, 2012, **108**, 056802.
11 Z. H. Qiao, W. Ren, H. Chen, L. Bellaiche, Z. Y. Zhang, A. H. MacDonald and Q. Niu, *Phys. Rev. Lett.*, 2014, **112**, 116404.
12 M. Ezawa, *Phys. Rev. Lett.*, 2012, **109**, 055502.
13 H. Pan, Z. S. Li, C. C. Liu, G. B. Zhu, Z. H. Qiao and Y. G. Yao, *Phys. Rev. Lett.*, 2014, **112**, 106802.
14 T. P. Kaloni, N. Singh and U. Schwingenschlogl, *Phys. Rev. B: Condens. Matter Mater. Phys.*, 2014, **89**, 035409.
15 P. Li, X. Li, W. Zhao, H. Chen, M. X. Chen, Z. X. Guo, J. Feng, X. G. Gong and A. H. MacDonald, *Nano Lett.*, 2017, **17**, 6195.
16 S. C. Wu, G. C. Shan and B. H. Yan, *Phys. Rev. Lett.*, 2014, **113**, 256401.
17 H. S. Zhang, T. Zhou, J. Y. Zhang, B. Zhao, Y. G. Yao and Z. Q. Yang, *Phys. Rev. B*, 2016, **94**, 235409.
18 P. Li, *Phys. Chem. Chem. Phys.*, 2019, **21**, 11150.
19 D. Xiao, W. G. Zhu, Y. Ran, N. Nagaosa and S. Okamoto, *Nat. Commun.*, 2011, **2**, 596.
20 Y. L. Wang, Z. J. Wang, Z. Fang and X. Dai, *Phys. Rev. B: Condens. Matter Mater. Phys.*, 2015, **91**, 125139.
21 P. Li and T. Y. Cai, *J. Phys. Chem. C*, 2020, **124**, 12705.
22 P. Li, Y. Ma, Y. Zhang and Z. X. Guo, *ACS Appl. Electron. Mater.*, 2021, **3**, 1826.
23 Z. F. Wang, Z. Liu and F. Liu, *Phys. Rev. Lett.*, 2013, **110**, 116801.
24 L. Dong, Y. Kim, D. Er, A. M. Rappe and V. B. Shenoy, *Phys. Rev. Lett.*, 2016, **116**, 096601.
25 X. M. Zhang, Z. H. Wang, M. W. Zhao and F. Liu, *Phys. Rev. B*, 2016, **93**, 165401.
26 X. L. Sheng and B. K. Nikolic, *Phys. Rev. B*, 2017, **95**, 201402(R).
27 C. X. Huang, J. Zhou, H. P. Wu, K. M. Deng, P. Jena and E. J. Kan, *Phys. Rev. B*, 2017, **95**, 045113.
28 Q. L. Sun and N. Kioussis, *Phys. Rev. B*, 2018, **97**, 094408.
29 P. Li, *Phys. Chem. Chem. Phys.*, 2019, **21**, 6712.

30 X. Y. Dong, J. F. Wang, R. X. Zhang, W. H. Duan, B. F. Zhu, J. O. Sofo and C. X. Liu, *Nat. Commun.*, 2015, **6**, 8517.
31 P. Li and T. Y. Cai, *Phys. Chem. Chem. Phys.*, 2020, **22**, 549.
32 C. Z. Chang, J. Zhang, X. Feng, J. Shen, Z. Zhang, M. Guo, K. Li, Y. Ou, P. Wei, L. L. Wang, Z. Q. Ji, Y. Feng, S. Ji, X. Chen, J. Jia, X. Dai, Z. Fang, S. C. Zhang, K. He, Y. Wang, L. Lu, X. C. Ma and Q. K. Xue, *Science*, 2013, **340**, 167.
33 X. Kou, S. T. Gou, Y. Fan, L. Pan, M. Lang, Y. Jiang, Q. Shao, T. Nie, K. Murata, J. Tang, Y. Wang, L. He, T. K. Lee, W. L. Lee and K. L. Wang, *Phys. Rev. Lett.*, 2014, **113**, 137201.
34 C. Z. Chang, W. Zhao, D. Kim, Y. H. Zhang, B. A. Assaf, D. Heiman, S. C. Zhang, C. Liu, M. H. W. Chan and J. S. Moodera, *Nat. Mater.*, 2015, **14**, 473.
35 Y. Deng, Y. Yu, M. Z. Shi, Z. Guo, Z. Xu, J. Wang, X. H. Chen and Y. Zhang, *Science*, 2020, **367**, 895.
36 A. Y. Lu, H. Y. Zhu, J. Xiao, C. P. Chuu, Y. Han, M. H. Chiu, C. C. Cheng, C. W. Yang, K. H. Wei, Y. Yang, Y. Wang, D. Sokaras, D. Nordlund, P. Yang, D. A. Muller, M. Y. Chou, X. Zhang and L. J. Li, *Nat. Nanotechnol.*, 2017, **12**, 744.
37 J. Zhang, S. Jia, I. Kholmanov, L. Dong, E. Er, W. Chen, H. Guo, Z. Jin, V. B. Shenoy, L. Shi and J. Lou, *ACS Nano*, 2017, **11**, 8192.
38 G. Kresse and J. Hafner, *Phys. Rev. B: Condens. Matter Mater. Phys.*, 1993, **47**, 558.
39 G. Kresse and D. Joubert, *Phys. Rev. B: Condens. Matter Mater. Phys.*, 1999, **59**, 1758.
40 J. P. Perdew, K. Burke and M. Ernzerhof, *Phys. Rev. Lett.*, 1996, **77**, 3865.
41 S. L. Dudarev, G. A. Botton, S. Y. Savrasov, C. J. Humphreys and A. P. Sutton, *Phys. Rev. B: Condens. Matter Mater. Phys.*, 1998, **57**, 1505.
42 F. Zhou, M. Cococcioni, C. A. Marianetti, D. Morgan and G. Ceder, *Phys. Rev. B: Condens. Matter Mater. Phys.*, 2004, **70**, 235121.
43 Y. S. Hou, H. J. Xiang and X. G. Gong, *Phys. Rev. B: Condens. Matter Mater. Phys.*, 2014, **89**, 064415.
44 A. Togo, F. Oba and I. Tanaka, *Phys. Rev. B: Condens. Matter Mater. Phys.*, 2008, **78**, 134106.
45 N. Marzari and D. Vanderbilt, *Phys. Rev. B: Condens. Matter Mater. Phys.*, 1997, **56**, 12847.
46 A. A. Mostofi, J. R. Yates, Y.-S. Lee, I. Souza, D. Vanderbilt and N. Marzari, *Comput. Phys. Commun.*, 2008, **178**, 685.
47 M. P. L. Sancho, J. M. L. Sancho and J. Rubio, *J. Phys. F*, 1984, **14**, 1205.
48 Q. S. Wu, S. N. Zhang, H.-F. Song, M. Troyer and A. A. Suluyanov, *Comput. Phys. Commun.*, 2018, **224**, 405.
49 F. P. Li, W. Wei, P. Zhao, B. B. Huang and Y. Dai, *J. Phys. Chem. Lett.*, 2017, **8**, 5959.
50 G. Henkelman, A. Arnaldsson and H. Jónsson, *Comput. Mater. Sci.*, 2006, **36**, 354.
51 N. D. Mermin and H. Wagner, *Phys. Rev. Lett.*, 1966, **17**, 1133.
52 W. B. Zhang, Q. Qu, P. Zhu and C. H. Lam, *J. Mater. Chem. C*, 2015, **3**, 12457.
53 Y. Y. Deng, Y. J. Yu, Y. C. Song, J. Z. Zhang, N. Z. Wang, Z. Y. Sun, Y. F. Yi, Y. Z. Wu, S. W. Wu, J. Y. Zhu, J. Wang, X. H. Chen and Y. B. Zhang, *Nature*, 2018, **563**, 94.
54 B. Huang, G. Clark, E. Navarro-Moratalla, D. R. Klein, R. Cheng, K. L. Seyler, D. Zhong, E. Schmidgall, M. A. McGuire, D. H. Cobden, W. Yao, D. Xiao, P. Jarillo-Herrero and X. Xu, *Nature*, 2017, **546**, 270.
55 Z. X. Guo and A. Oshiyama, *Phys. Rev. B: Condens. Matter Mater. Phys.*, 2014, **89**, 155418.
56 P. Li, J. X. Cao and Z. X. Guo, *J. Mater. Chem. C*, 2016, **4**, 1736.
57 Z. X. Guo, S. Furuya, J. Iwata and A. Oshiyama, *Phys. Rev. B: Condens. Matter Mater. Phys.*, 2013, **87**, 235435.
58 C. Zhong, W. Wu, J. He, G. Ding, Y. Liu, D. Li, S. Yang and G. Zhang, *Nanoscale*, 2019, **11**, 2468.
59 D. Xiao, M. C. Chang and Q. Niu, *Rev. Mod. Phys.*, 2010, **82**, 1959.
60 X. Wang, J. Yates, I. Souza and D. Vanderbilt, *Phys. Rev. B: Condens. Matter Mater. Phys.*, 2006, **74**, 195118.
61 M. L. Sancho, J. L. Sancho, J. L. Sancho and J. Rubio, *J. Phys. F*, 1985, **15**, 851.
62 I. Souza, N. Marzari and D. Vanderbilt, *Phys. Rev. B: Condens. Matter Mater. Phys.*, 2001, **65**, 035109.
63 Y. Hatsugai, *Phys. Rev. Lett.*, 1993, **71**, 3697.